Projected Future Changes of Tropical Cyclone Activity over the Western North and South Pacific in a 20-km-Mesh Regional Climate Model

CHUNXI ZHANG

International Pacific Research Center, School of Ocean and Earth Science and Technology, University of Hawai'i at Mānoa, Honolulu, Hawaii

YUQING WANG

International Pacific Research Center, and Department of Atmospheric Sciences, School of Ocean and Earth Science and Technology, University of Hawai'i at Mānoa, Honolulu, Hawaii

(Manuscript received 14 August 2016, in final form 16 April 2017)

ABSTRACT

A high-resolution regional atmospheric model is employed to project the late twenty-first-century changes of tropical cyclone (TC) activity over the western North Pacific (WP) and southwest Pacific (SP). The model realistically reproduces the basic features of the TC climatology in the present-day simulation. Future projections under the representative concentration pathway 4.5 (RCP45) and 8.5 (RCP85) scenarios are investigated. The results show no significant change of TC genesis frequency (TCGF) in the WP by RCP45 due to the cancellation of the reduction over the western part and the increase over the eastern part together with a considerable decrease of TCGF by RCP85 due to the excessive TCGF reduction in the western part. The TCGF over the SP consistently decreases from RCP45 to RCP85. Despite the fact that the simulated maximum surface wind speeds are below 52 m s^{-1}, the change with more strong TCs and fewer weak TCs is robust. The future changes in the TC genesis locations and translational speeds modulate the TC lifetime and frequency of occurrence. The TC genesis potential index (GPI) is used to evaluate the projected TCGF changes. The results show that low-level vorticity and midtropospheric vertical velocity largely contribute to the reduction of GPI in the western part of the WP, while vertical wind shear and midtropospheric vertical velocity mainly contribute to the decrease of GPI over the SP. The weakening of the monsoon trough is found to be responsible for the decreases of GPI and TCGF over the western part of the WP.

1. Introduction

The tropical cyclone (TC) activity over the western North Pacific (WP) will likely change in a future warmer world (Oouchi et al. 2006; Stowasser et al. 2007; Yokoi and Takayabu 2009; Zhao et al. 2009; Li et al. 2010; Knutson et al. 2010; Murakami et al. 2011, 2012; Held and Zhao 2011; Sugi et al. 2012; Yokoi et al. 2012; Emanuel 2013; Colbert et al. 2015; Wu et al. 2014; Manganello et al. 2014). However, the projected future TC activity is diverse due to different models, methods, and scenarios applied. Many previous studies predicted a future decrease in TC genesis frequency and an increase in intense TCs (e.g., Oouchi et al. 2006; Bengtsson et al. 2007a,b; Zhao et al. 2009; Murakami et al. 2011, 2012; Sugi et al. 2012; Wu et al. 2014). Nevertheless, some studies have shown contrasting future projections. Emanuel (2013) found that both TC frequency and intensity increase over the WP in the late twenty-first century based on downscaling the phase 5 of the Coupled Model Intercomparison Project (CMIP5) climate models under the representative concentration pathway 8.5 scenario, whereas Stowasser et al. (2007) found no statistically significant change of TC frequency in the peak season from July to October in response to the carbon dioxide increase over the WP. By contrast, the TC activity over the southwest Pacific (SP) is less widely studied and the conclusions are more consistent among different studies (e.g., the projected TC frequency will decrease) (Zhao et al. 2009; Lavender and Walsh 2011; Murakami et al. 2012; Emanuel 2013; Walsh 2015).

Most of the general circulation models (GCMs) have low horizontal resolutions, such as the phase 3 of the

Corresponding author: Prof. Yuqing Wang, yuqing@hawaii.edu

DOI: 10.1175/JCLI-D-16-0597.1

Coupled Model Intercomparison Project (CMIP3) and phase 5 (CMIP5) models. Regardless of the disability to simulate the complex inner core of intense TCs, those models still provided credible future climate projections to a certain degree (Bengtsson et al. 2007b; Villarini and Vecchi 2012; Camargo 2013). The high-resolution GCMs, on the other hand, are capable of adequately resolving TCs. In the last few years, some research centers have started to run high-resolution GCMs to produce more realistic TC characteristics (Oouchi et al. 2006; Bengtsson et al. 2007a,b; Zhao et al. 2009; Murakami et al. 2012; Kinter et al. 2013) with the prescribed sea surface temperature (SST). The 20-km resolution Meteorological Research Institute (MRI) atmospheric general circulation model (MRI-AGCM) was successfully configured to study the TC climatology and future projections (Murakami et al. 2012). There are very strong TCs in their simulations due to the use of the improved cumulus parameterization scheme. Recently a comparison among different dynamical cores has demonstrated that the dynamical core has a significant impact on storm intensity and genesis frequency in the Community Atmosphere Model version 5 (CAM5; Reed et al. 2015). The spectral element core produces stronger TCs than the finite-volume core by using very similar parameterization packages. These findings might be an additional explanation for why Murakami et al. (2012) can simulate very strong TCs. The Geophysical Fluid Dynamics Laboratory (GFDL) High Resolution Atmospheric Model (HiRAM) is another GCM widely used to study TC climatology and future projections (e.g., Zhao et al. 2009; Held and Zhao 2011; Knutson et al. 2015). The HiRAM was developed based on the GFDL Atmospheric Model version 2.1 with increased horizontal and vertical resolutions, as well as simplified parameterizations for moist convection in order to better represent TC climatology (Zhao et al. 2009).

Compared with GCMs, regional climate models (RCMs) can save numerous computing resources yet still provide detailed information on TC activity in a region of interest, and hence are widely used to study TC climatology and future projections. The pioneering work was carried out by Knutson et al. (1998) and Knutson and Tuleya (2004). They tracked each TC identified back to its genesis and early development stage in coarse-resolution GCMs, and then ran each storm case by a multiply nested limited-area atmospheric model with 18- or 9-km horizontal resolution. Stowasser et al. (2007) used a regional climate model with horizontal resolution of half degree developed at the International Pacific Research Center (IPRC-RegCM; Wang et al. 2003) to study possible changes in TC activity over the western North Pacific with increased CO_2 concentration. The GFDL's Regional Atmospheric Model with 18-km horizontal resolution was first configured by Knutson et al. (2007) to study the recent multidecadal change of Atlantic hurricane activity. This model has been then applied to study the projected changes in TC activities in the future warmer world over the North Atlantic (e.g., Knutson et al. 2008, 2010) as well as over the WP (Wu et al. 2014) and SP (Walsh 2015).

The Weather Research and Forecasting (WRF) Model has been limited to a small number of studies on TC climatology and/or future projections for the WP or the SP (e.g., Jourdain et al. 2011; Jullien et al. 2014; Kim et al. 2015; Jin et al. 2016). A recent evaluation of the climatology of TC activity over the WP in the Coordinated Regional Climate Downscaling Experiment (CORDEX) showed that the WRF-based RCM is capable of reproducing the TC climatology (Jin et al. 2016). Similar results were reported in a WRF-based RCM simulation by Kim et al. (2015). Both simulations used 50-km horizontal resolution and Kain–Fritsch cumulus parameterization (CP) scheme (Kain 2004). More recent studies have shown that the Kain–Fritsch CP scheme in the WRF Model is sensitive to the horizontal resolution (Done et al. 2015; Hashimoto et al. 2016); that is, the TC frequency increases with the increasing model resolution. This sensitivity is also found in the European Centre for Medium-Range Weather Forecasts (ECMWF) Integrated Forecast System (IFS) model with the Tiedtke CP scheme (Manganello et al. 2012). The simulated TC climatology has been reported to be sensitive to the CP scheme in other studies as well (e.g., Knutson and Tuleya 2004; Murakami et al. 2012). In this study, we first implemented a new version of the Tiedtke scheme that was tested for 20-km horizontal resolution. We then apply the 20-km-grid WRF-based RCM to study the TC climatology and future projections over the WP and the SP. The study aims to investigate the following:

1) How well the WRF Model with the new Tiedtke scheme can capture the present-day (PD) TC climatology over the WP and the SP, e.g., the intensity, the geographical distribution, the seasonal cycle, and the interannual variations. We noticed that many previous studies used spectral nudging in the dynamical downscaling to keep the RCM simulated large-scale state close to the driving fields (e.g., Wu et al. 2014; Jin et al. 2016; Walsh 2015;). Here, we will show that the WRF Model with the new Tiedtke scheme can capture the PD climatology of TC activity without the use of spectral nudging.
2) The TC activity over the WP and the SP in response to the future warmer climate in the late twenty-first

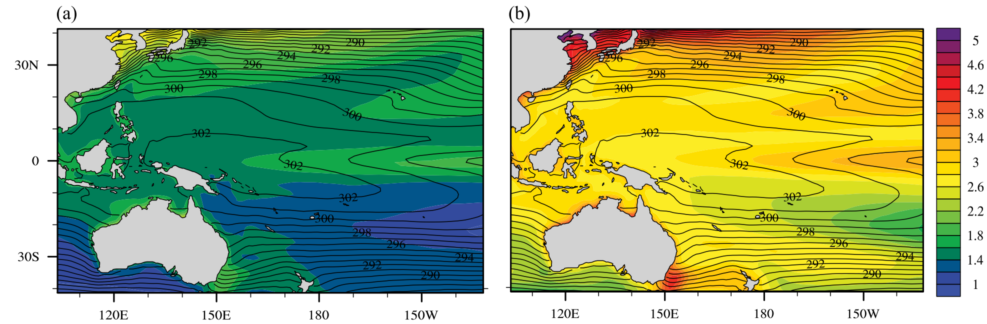

FIG. 1. The observed SST (contour, K) and multimodel ensemble mean increments of SST for (a) RCP4.5 and (b) RCP8.5 scenarios.

century. Two projected simulations forced with specified concentrations consistent with a high-emission scenario and a medium-emission scenario are performed, whereas most previous studies mainly evaluated only one scenario for the WP or the SP (Zhao et al. 2009; Murakami et al. 2011, 2012; Wu et al. 2014; Walsh 2015).

The rest of the paper is organized as follows. Section 2 describes the data, model, and experimental design. Section 3 presents the comparison of the simulated PD TC climatology with observations, and the projected future changes. The possible mechanisms for the future change of TC activity are discussed in section 4. The main results are summarized in section 5. The details of the new modified Tiedtke cumulus parameterization scheme are briefly noted in the appendix.

2. Data and methodology

a. Data

The International Best Track Archive for Climate Stewardship (IBTrACS) World Meteorological Organization version v03r05 provides TC best-track data to aid the understanding of distribution, frequency, and intensity of TCs worldwide (Knapp et al. 2010). It includes the central position, maximum sustained near surface wind speed, and minimum central sea level pressure (SLP) for each TC globally at 6-h intervals. Since IBTrACS is a compilation of data from many agencies, the IBTrACS maximum sustained wind is an average from all available agencies and will likely be different from the reports of each agency. The model results from the present-day (PD) simulation (see below) will be evaluated against this dataset.

The National Ocean and Atmosphere Administration (NOAA) global daily SST analysis with the horizontal resolution of 0.25° longitude × 0.25° latitude (Reynolds et al. 2010) was used to give the lower boundary condition over the ocean for the regional atmospheric model. The National Aeronautics and Space Administration's (NASA) Modern-Era Retrospective Analysis for Research and Applications (MERRA) reanalysis data with horizontal resolution of 0.5° latitude × ⅔° longitude (Rienecker et al. 2011) were used to provide both initial and lateral boundary conditions for the model atmosphere. The ECMWF interim reanalysis (ERA-Interim) data with a horizontal resolution of around 0.75° in both longitude and latitude (Dee et al. 2011) were used to give the initial soil moisture and soil temperature to the land surface model described below.

b. Model and experimental design

We used the Weather Research and Forecasting Model version 3.6 to conduct the numerical experiments (Skamarock et al. 2008). The domain covers the central to western tropical and subtropical Pacific (Fig. 1). The horizontal resolution is 20 km on a Mercator projection. There are 51 vertical levels from the surface to the model top at 10 hPa. The outer 10 grid points in the outermost domain are treated as a buffer zone in which the results are relaxed to values interpolated in time and space from the 6-h snapshots provided by the NASA MERRA reanalysis. No spectral nudging is applied in the model. The SST is prescribed and updated daily using the NOAA global analysis. The model integration for the PD run started at 0000 UTC 1 December 1989 and ended on 0000 UTC 1 January 2010. The initial conditions for the atmosphere are also from NASA MERRA reanalysis data, but the soil moisture and soil temperature at the initial time are taken from the ERA-Interim data. Note that the first month is considered the model spinup period and discarded in the following analysis.

The WRF single-moment six-class (WSM6) microphysics scheme (MP) with six prognostic cloud variables

TABLE 1. The CMIP5 models used for the ensemble mean increments. (Expansions of acronyms are available online at http://www.ametsoc.org/PubsAcronymList.)

Originating group(s)	Country	CMIP5 I.D.
CSIRO (Commonwealth Scientific and Industrial Research Organization, Australia), and BOM (Bureau of Meteorology, Australia)	Australia	ACCESS1.0
Beijing Climate Center, China Meteorological Administration	China	BCC-CSM1.1
Canadian Centre for Climate Modeling and Analysis	Canada	CanESM2
Geophysical Fluid Dynamics Laboratory	United States	GFDL-CM3
NASA Goddard Institute for Space Studies	United States	GISS-E2-R
Met Office Hadley Centre (additional HadGEM2-ES realizations contributed by Instituto Nacional de Pesquisas Espaciais)	United Kingdom	HadGEM2-CC
Institute for Numerical Mathematics	Russia	INM-CM4
Institut Pierre-Simon Laplace	France	IPSL-CM5A-LR
Atmosphere and Ocean Research Institute (The University of Tokyo), National Institute for Environmental Studies, and Japan Agency for Marine-Earth Science and Technology	Japan	MIROC5
Japan Agency for Marine-Earth Science and Technology, Atmosphere and Ocean Research Institute (The University of Tokyo), and National Institute for Environmental Studies	Japan	MIROC-ESM
Meteorological Research Institute	Japan	MRI-CGCM3
Norwegian Climate Centre	Norway	NorESM1-M

is used for grid-scale cloud microphysics processes (Hong and Lim 2006). The shortwave and longwave radiation fluxes are calculated using the RRTMG radiation scheme (Iacono et al. 2008). The Yonsei University (YSU) planetary boundary layer (PBL) scheme (Hong et al. 2006) is used for subgrid-scale vertical mixing. The Noah land surface model (LSM) is used for the land surface processes (Chen and Dudhia 2001). We applied a new Tiedtke scheme for cumulus parameterization (cu_physics = 16 in WRF since version 3.7; see the appendix for a brief description).

Besides the PD run, two future runs are conducted. For the future runs, we used the pseudoglobal warming (PGW) method (Sato et al. 2007; Kimura and Kitoh 2007; Knutson et al. 2008; Kawase et al. 2009; Lauer et al. 2013) and simulations of the CMIP5 for RCP4.5 and 8.5 scenarios in the late twenty-first century (e.g., 2080–99; hereafter, we name these two future runs RCP45 and RCP85, respectively). By the PGW method, both the initial and boundary conditions for the regional model integrations are given by the sum of observations (reanalysis data and observed SSTs) and a perturbation or global warming increment constructed from simulations of global coupled models (e.g., CMIP5). The future increments for atmospheric components (e.g., 3D temperature, geopotential height, winds, specific humidity) and SST are obtained from the CMIP5 multimodel ensemble means (e.g., the late twenty-first-century minus the PD simulations for the multimodel ensemble means from the CMIP5 models). The monthly future increments are interpolated into 6-h intervals and added to the PD driving fields. Hence, the synoptic and interannual variabilities at the lateral boundaries of the outermost model domain and for SST are the same for the PD run and the future runs. More detailed discussions of the PGW method are presented in Lauer et al. (2013) and Zhang et al. (2016a,b). Twelve CMIP5 models (for both RCP45 and RCP85 scenarios) used in our study are listed in Table 1. The selection of these 12 models was based on the availability of the atmospheric output variables. We chose one model from each available research center only if there were more than one model available. Figure 1 shows the multimodel ensemble mean increments for SST (shading) from CMIP5 climate models for RCP45 (Fig. 1a) and RCP85 (Fig. 1b), respectively. The contour shows the climatological SST from the NOAA global analyses. The SST increments are asymmetric between the WP and the SP, around 1.6 K over the WP and 1.2 K over the SP for RCP45, and around 3 K over the WP and 2.4 K over the SP for RCP85.

c. *Analysis methods*

1) TC TRACKING ALGORITHM

In this study, we used the 6-h model outputs to identify and track TCs. The algorithm used the following four criteria based on those reported in Nguyen and Walsh (2001) but with some modifications in order to match the 20-km horizontal resolution. 1) The maximum relative vorticity at 850 hPa exceeds $2.0 \times 10^{-4}\,s^{-1}$. 2) There is a minimum SLP center with closed isobar within the radius of 300 km of the maximum relative vorticity center at 850 hPa. The radius of the averaged minimum SLP system is at least 100 km. The closed isobar drops at least 1 hPa to the minimum SLP center. 3) There is a warm core within 300 km of the minimum SLP center and the warm core has the temperature within the 100-km radius at least 0.1 K warmer than the temperature between 100 and 300 km averaged between 700 and 300 hPa. 4) The maximum 10-m wind speed in the lifetime is larger than 17 m s^{-1} and the genesis time is defined as the time when the maximum 10-m wind speed reaches 17 m s^{-1}. The duration of each detected storm must exceed 48 h.

2) PAIRED *T* TEST

We used a Student's *t* test to check if the differences between the PD run and future run are statistically significant. Our null hypothesis is that the PD run and the future run have the same climatological mean value. Since we consider the possibility of either positive or negative differences, we employed a ''double-tailed'' *t* test. Furthermore, since the PD run and the future run use the same base years (with and without adding the global warming increments), we applied a ''paired'' *t* test (e.g., McDonald 2014). We applied the test to the time series of the annual means at each grid point.

3) BOOTSTRAP TEST

The bootstrap method is applied to test if the future changes in TC genesis frequency, occurrence frequency, and accumulated cyclone energy (ACE) are significant (e.g., Fig. 5), given the fact that the values at each grid cell do not follow a Gaussian distribution. The bootstrapping procedure is provided by NCAR Command Language (http://www.ncl.ucar.edu).

4) GENESIS POTENTIAL INDEX

We used the modified version of Emanuel and Nolan's (2004) TC genesis potential index (GPI; Murakami and Wang 2010) to study factors that influence the changes of TC genesis,

$$\mathrm{GPI} = |10^5\eta|^{3/2}\left(\frac{\mathrm{RH}}{50}\right)^3\left(\frac{V_{\mathrm{mpi}}}{70}\right)^3 \times(1+0.1V_{\mathrm{sh}})^{-2}\left(\frac{-\omega+0.1}{0.1}\right), \qquad (1)$$

where η is the absolute vertical vorticity (s^{-1}) at 850 hPa, RH is the relative humidity (percentage) at 700 hPa, V_{mpi} is the maximum potential intensity (MPI; m s^{-1}, Emanuel 1995), V_{sh} is the magnitude of the vertical wind shear (m s^{-1}) between 850 and 200 hPa, and ω is the vertical *p* velocity (Pa s^{-1}) at 500 hPa. The code to calculate the MPI is available online at ftp://texmex.mit.edu/pub/emanuel/TCMAX//pcmin_revised.f. There are five factors in the GPI formula in total. We varied each factor at one time to check the contribution of each individual factor to the future change of GPI, for example,

$$\Delta\mathrm{GPI}_i = \Delta F_i \times (F_{j1}\times F_{j2}\times F_{j3}\times F_{j4}), \qquad (2)$$

where Δ represents the future change (e.g., RCP45 or RCP85 minus PD). The subscript *i* is the contributing factor, and subscripts *j*1 to *j*4 are the remaining factors in PD.

3. Climatology and future change

a. *TC tracks*

The observed and simulated TC tracks are shown in Fig. 2. Note that the WP (0°–39.5°N, 110°E–140°W) and the SP (0°–39.5°S,145°E–140°W) are defined by our domain settings in this study rather than as commonly defined. Note that the WP includes part of the central North Pacific. The observed annual mean TC number is 25.9 over the WP (Fig. 2a). The same number is simulated in the PD run (Fig. 2b). By contrast, the model overpredicts nearly 3 TCs in the annual mean over the SP (Figs. 2a,b). The annual mean TC number does not change over the WP in the RCP45 run (Fig. 2c), but is reduced by more than 4 in the RCP85 run. Over the SP, the annual mean TC number decreases in the warmed climates (Figs. 2c,d) and is only 4.2 in the RCP85 run.

b. *TC intensity*

Similar to the results from previous studies using regional models, the simulated TC intensity at around 20-km resolution is not as strong as the observed (e.g., Knutson et al. 2007; Wu et al. 2014; Walsh 2015). The strongest TC in our simulations has a maximum 10-m wind speed of 52 m s^{-1}. Figures 3a and 3b show the annual mean TC frequency versus maximum surface wind speed based on the 6-h interval data for the WP and SP, respectively. Compared to the observations, the simulated TCs in the PD run show more frequent wind speeds lower than 37.5 m s^{-1}, but less frequent wind speeds higher than 37.5 m s^{-1} for both the WP and the SP (Figs. 3a,b). Compared to the PD run, there are less frequent wind speeds lower than 42.5 m s^{-1}, but more frequent wind speeds higher than 42.5 m s^{-1} for both RCP45 and RCP85 runs over the WP. The frequency of TCs for most of intensity bins is reduced mainly due to the significant reduction of TC genesis number in the future runs (RCP45 and RCP85) over the SP. The change is statistically significant especially for RCP85 at most of wind speeds. The basic conclusion of fewer weak TCs but more strong TCs over the WP in the warmer

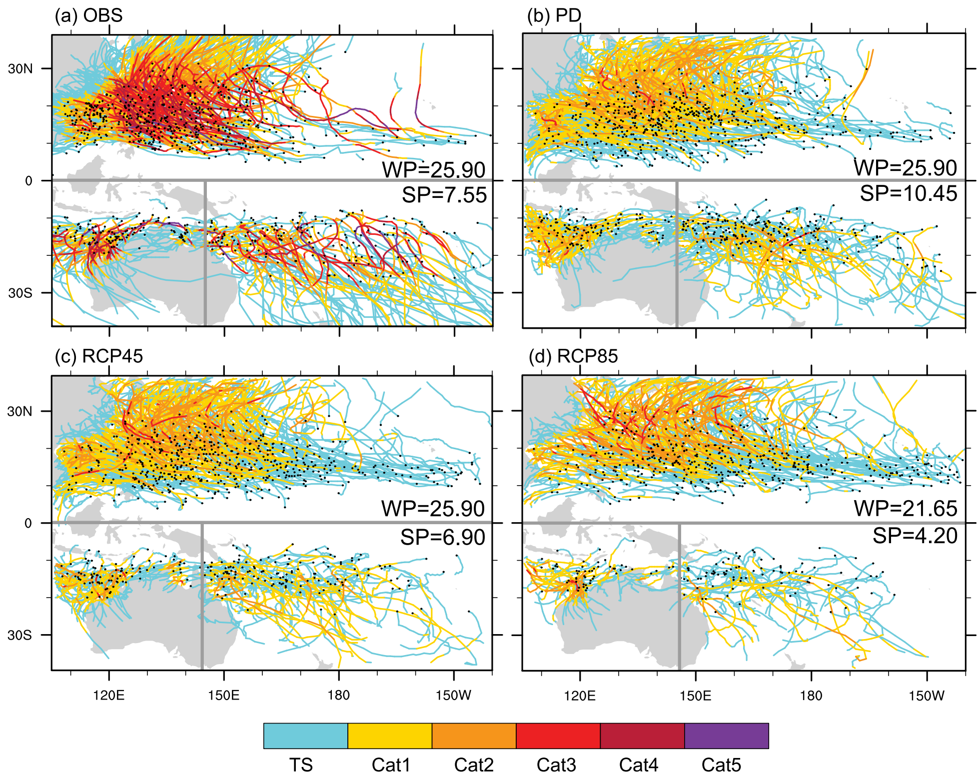

FIG. 2. The (a) observed and (b)–(d) simulated TC tracks in the present-day (PD), RCP45, and RCP85 runs, respectively. The TC intensity is classified by tropical storms (TS) and category 1 (CAT1) to category 5 (CAT5) with Saffir–Simpson hurricane wind scale. The dots are the TC genesis locations. The annual mean TC numbers are shown in the corresponding panels. The wind speed in IBTrACS data is divided by 0.88 in order to get category 4 and 5 TCs.

climate is consistent with that of Murakami et al. (2012), who found that the TC frequency decreases for weak TCs but slightly increases for strong TCs (see their Fig. 8) over the Northern Hemisphere.

For the lifetime maximum surface wind speed, there are more weak TCs and fewer strong TCs compared to the observations for both the WP and the SP (Figs. 3c,d). Compared with the PD run, in the future runs, there will be more strong TCs for both RCP45 and RCP85 over both the WP and the SP. In comparison to the RCP45 run, the RCP85 run has higher ratio of strong TCs, indicating a tendency of more strong TCs while less weak TCs with more warming over the WP and SP (Figs. 3e,f). The future change of the lifetime maximum surface wind speed over both the WP and the SP is consistent with the findings by Knutson et al. (2015, see their Fig. 6a) in spite of the fact that their results are for all TC basins. In their study, the frequency change is significant in downscaled simulations at the 6-km resolution, but not significant in their global 50-km resolution simulations.

c. Seasonal cycle and interannual variation of TC genesis frequency

The interannual variations of TC genesis frequency over the WP (Fig. 4a) and the SP (Fig. 4b) are reasonably captured in the PD run. The correlation coefficient between the PD run and the observations over the WP is 0.58, which is statistically significant at the 95% confidence level. The TC genesis number from the PD run over the WP is also correlated to that from the RCP45 and RCP85 runs, statistically significant at the 95% confidence level. The correlation coefficient between the PD run and the observations over the SP is 0.61, which is statistically significant at the 99% confidence level (Fig. 4b). However, the PD interannual variation of TC frequency is not well correlated with the RCP45 and RCP85 runs. Keep in mind that we used the same SST distribution patterns and the same driving fields at the lateral boundary for the PD run and the warming runs except that the warming signals were added as perturbations to the SST and the driving fields for the

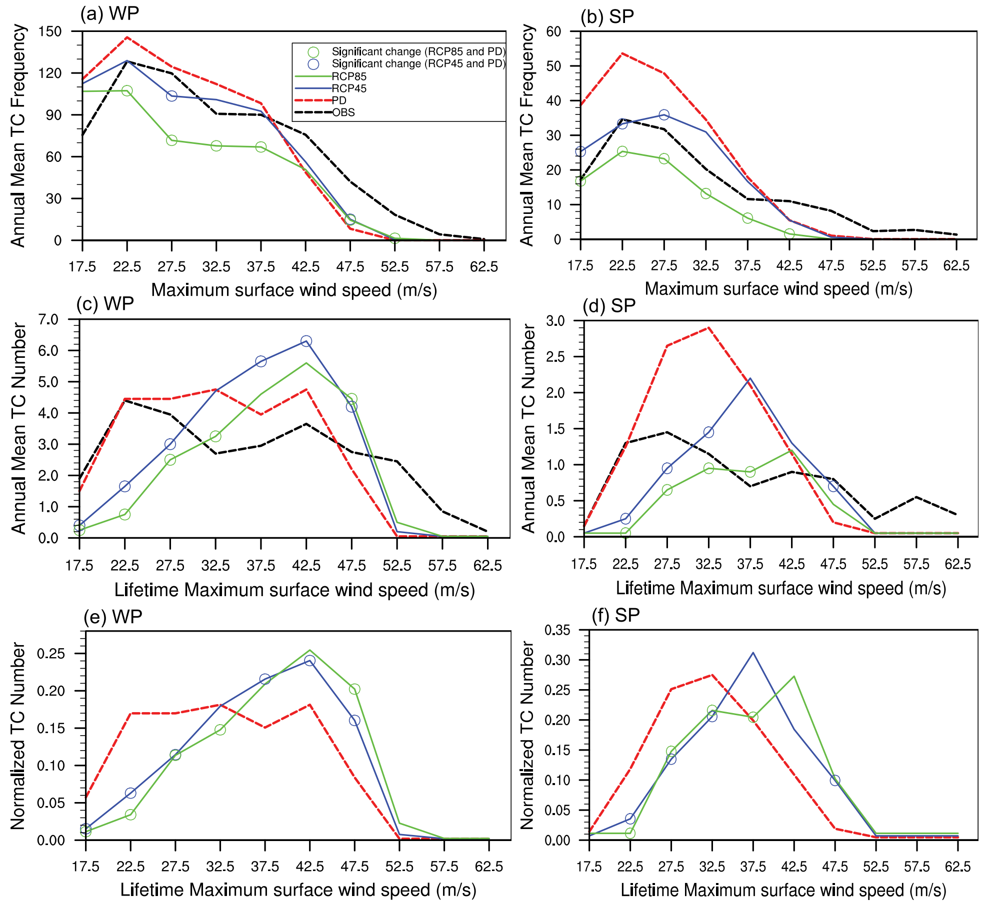

FIG. 3. The annual mean frequency of occurrence for maximum surface wind speed for TCs over the (a) WP and (b) SP, and (c)–(f) the annual mean or normalized TC number for the lifetime maximum surface wind speed for the WP and SP. The frequency of occurrence for maximum surface wind speed is accumulated in 6-h intervals. The circles indicate the future change being statistically significant at the 90% confidence level.

future runs. The model domain is large enough to produce different annual TC frequencies in the future runs from the PD run. Note also that the correlation coefficient can be influenced by the definition of the WP and the SP in this study.

Figures 4c and 4d show the seasonal variations of TC genesis numbers over the WP and the SP, respectively. The peak month from observation is August for the WP, whereas the PD run peaks in September, one month later (Fig. 4c). The PD run obviously overestimates TCs in September and October over the WP but underestimates TCs in all other months. The future change is only significant in June for RCP45, and June, July, and December for RCP85 over the WP. January, February, and March are all peak months over the SP. The PD run overestimates the TC genesis frequency almost in all months with the peak month in March. There are fewer occasions of TC genesis in all months in the future runs by the late twenty-first century over the SP. Only the changes in March and December are statistically significant for RCP45, whereas the changes are statistically significant from December to April for RCP85 over the SP at the 90% confidence level.

d. Annual mean genesis frequency, frequency of occurrence, and accumulated cyclone energy

As mentioned in section 2, the TC genesis is defined by the time when the 10-m wind speed reaches 17 m s^{-1} in our study. The TC genesis frequency of each 5° × 5° grid box is the 20-yr mean of TC genesis numbers in the box. Figure 5a shows the observed annual mean genesis frequency (shading) and the simulated genesis frequency in the PD run (contour). The simulated PD genesis frequency distribution over the WP is similar to

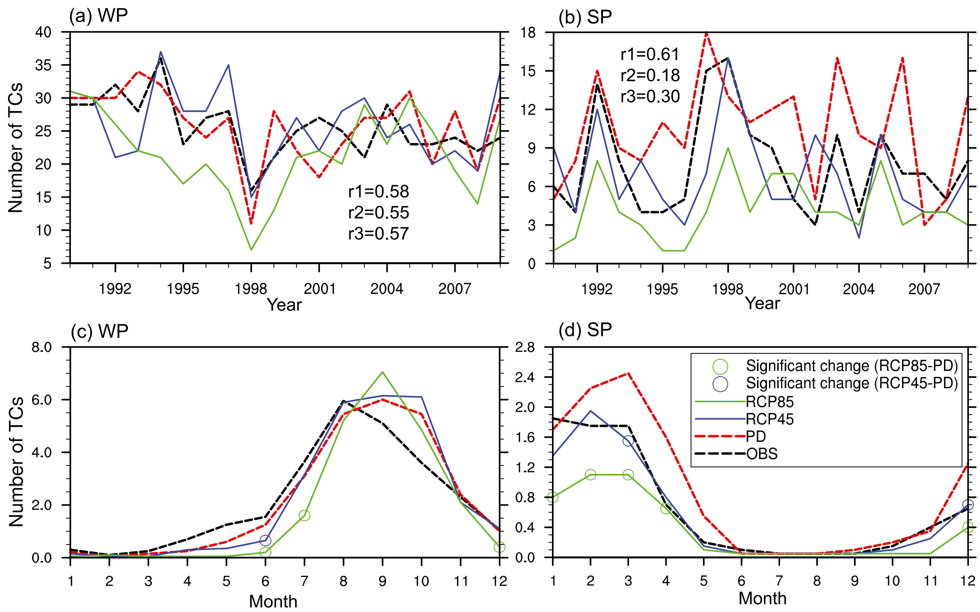

FIG. 4. The interannual variation in annual TC numbers over the (a) WP and (b) SP; r1 means the correlation coefficient between observations and the PD run, r2 means the correlation coefficient between the PD and RCP45 runs, and r3 means the correlation coefficient between the PD and RCP85 runs. (c),(d) The seasonal cycle in monthly TC genesis number over the WP and SP, respectively. The circles indicate the future change being statistically significant at the 90% confidence level.

the observed. The maximum annual mean TC genesis number is around 0.8 in the PD simulation, which agrees well with that in observation, but the center of the maximum annual mean TC genesis frequency is located between 140° and 160°E, which is about 15 degrees east of the observed center. There is also overly strong genesis in the central North Pacific close to Hawaii in the PD simulation. Although the TC genesis locations are similar in the PD simulation and the observation over the SP, the PD simulation obviously overestimates the TC genesis number. It is clearly seen that in the future runs (Figs. 5b,c), the TC genesis frequency decreases west of 165°E and increases east of 165°E over the WP. The TC genesis frequency widely decreases over the SP in both future warming scenarios. The vertical lines in Fig. 5b are the average TC genesis longitude for the PD (black), RCP45 (green), and RCP85 (red) runs, respectively. The TC genesis locations shift eastward over the WP and westward over the SP. The green dots in Fig. 5 indicate the future change that is statistically significant at the 90% confidence level. The change is more significant for the RCP85 scenario.

In each 5° × 5° grid box, we count the frequency of TC occurrence at every 6 h. Figure 5d shows the 20-yr mean TC occurrence frequency. The TC occurrence frequency in the PD run (contour) is very similar to that in observation (shading) over the WP in terms of the distribution and magnitude. The location of the maximum TC occurrence frequency in the PD run is about 5 degrees south and southeast of that from observation (Fig. 5d). There are slightly more TCs east of 180° in the PD run (Fig. 5d). In spite of the distribution of TC occurrence frequency being well simulated in the PD run over the SP, the simulated PD occurrence frequency is much higher than the observed (Fig. 5d). Too many TCs and too long-lived TCs (not shown) in the PD run account for the large positive bias in the simulated TC occurrence frequency over the SP. Similar to the TC genesis frequency, the TC occurrence frequency is higher east of 165°E and lower west of 165°E over the WP for both the RCP45 and RCP85 scenarios (Figs. 5e,f), which is more significant in the RCP85 run. Different from the WP, the TC occurrence frequency almost homogeneously decreases over the SP (Figs. 5e,f). The distribution of the accumulated cyclone energy (Fig. 5g) is very similar to the TC occurrence frequency (Fig. 5d) in observations and in the PD run, where ACE ($\sum V_{\max}^2$, $V_{\max}$ is maximum 10-m wind speed) is calculated for each grid cell at each time interval along a track and for all TCs in each season for the 20-yr period. The magnitude in the PD run is smaller than that in observations because the simulated TCs are weaker.

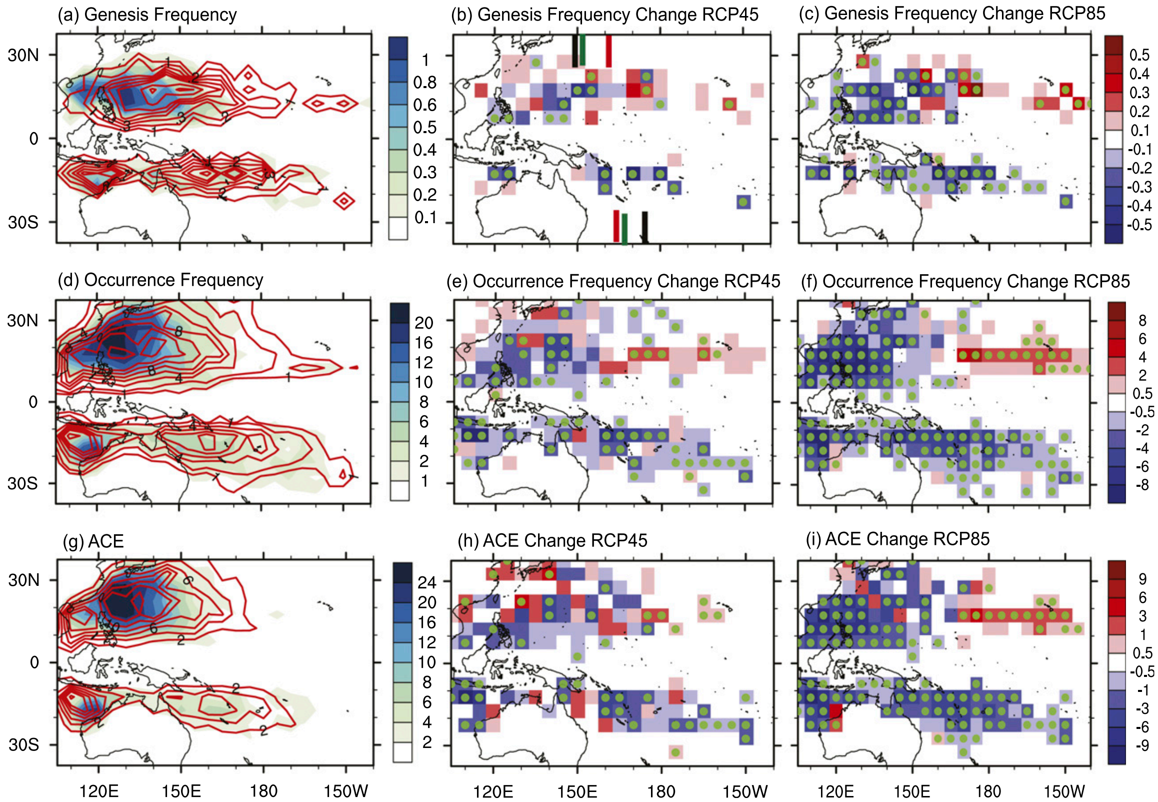

FIG. 5. (left) The annual mean (a) TC genesis frequency, (d) frequency of occurrence, and (g) ACE during 1990–2009. The contours are for the PD run, while the shading is for observations. The contour has the same interval as the shading. (middle),(right) Future change for annual TC (b),(c) genesis frequency, (e),(f) frequency of occurrence, and (h),(i) ACE, for RCP45 and RCP85, respectively. The TC genesis locations were counted in every 5° × 5° grid box. The TC locations and ACE were counted in every 5° × 5° grid box with 6-h intervals. The unit for ACE is $10^3\,m^2\,s^{-2}$. The green dots in indicate the future change being statistically significant at the 90% confidence level. The vertical lines in (b) represent the averaged TC genesis longitudes for the PD (black), RCP45 (green), and RCP85 (red) runs.

The future change of ACE is also similar to the TC occurrence frequency (Figs. 5e,f,h,i). Note that both occurrence frequency and ACE increase in both RCP45 and RCP45 scenarios near the Hawaiian Islands, suggesting that the region could experience effect of more TCs in the future warmer climate. Similar results are also reported in Murakami et al. (2013) and Knutson et al. (2015).

4. Discussion

a. Changes in TC occurrence frequency

As shown in Fig. 4c, July to October (JASO) is the peak season for TC genesis and occurrence over the WP, and January to April (JFMA) is the peak season for the SP (Fig. 4d). Hence, we will focus our discussion on JASO for the WP and JFMA for the SP in this section. Changes in TC occurrence frequency can be explained by changes in both TC genesis locations and motions. There will be a significant reduction in TC genesis frequency over the western part of the WP (e.g., west of 165°E) and a significant increase over the eastern part of the WP (Figs. 5b,c). If the TCs that formed in the eastern part of the WP kept moving westward, the TC occurrence frequency over the western part would not significantly decrease. However, the TCs that formed over the eastern part of the WP move northward and usually fast. Figures 6a and 6b compare the mean TC translation vectors between the PD run and observations. The mean TC translation vectors are calculated at every 5° × 5° grid box. Note that only those grids with annual mean TC occurrence frequency larger than 1 are shown in the figure. Overall, the PD run successfully captured the motion direction and speed of TCs. The mean TC motion speeds over the WP are 5.4, 5.5, and 5.7 $m\,s^{-1}$ for the PD, RCP45, and RCP85 runs, respectively, indicating a slightly increased TC motion speed in the projected

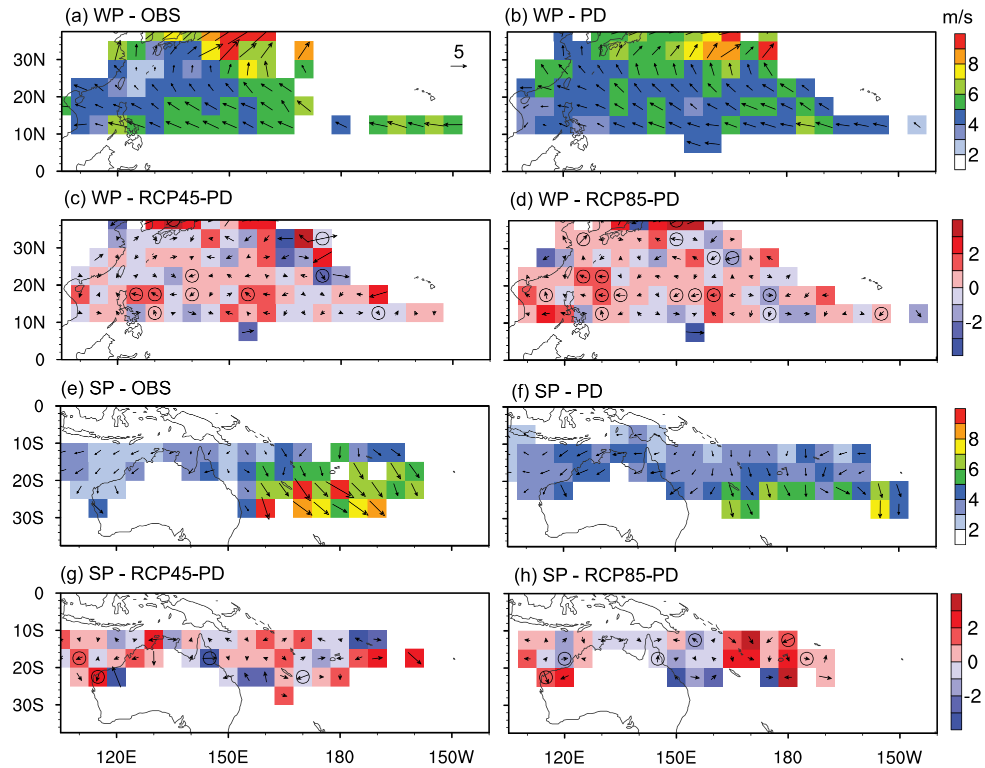

FIG. 6. The (a),(e) observed and (b),(f) simulated PD mean TC translation vectors and magnitudes (shading) for the peak TC season [JASO over the WP in (a) and (b) and JFMA over the SP in (e) and (f)]. (c),(g) The difference between the RCP45 and PD runs for the WP and the SP, respectively. (d),(h) As in (c),(g), but for RCP85. The black circles in (c), (d), (g), and (h) indicate that the vector difference of either the zonal or meridional component is statistically significant at the 90% level.

future runs on average (see also Figs. 6c,d). The TCs are projected to move faster in the western part of the WP ($5.8\,\mathrm{m\,s^{-1}}$) than in the eastern part of the WP ($5.5\,\mathrm{m\,s^{-1}}$) for RCP85 run. The future changes in the mean zonal motion speed are -0.02 and -0.31 (the change is statistically significant at the 90% confidence level) in the RCP45 and RCP85 runs, respectively, indicating that TCs would move slightly faster toward the west in the warmer climate. The future changes of the zonal speed over the western part of the WP are larger (-0.39) than over the eastern part of the WP (-0.22) for the RCP85 run. The future changes in the mean meridional motion component are relatively small for both the RCP45 and RCP85 runs. As a result, the mean lifetime of TC decreases by 0.41 days in the RCP45 run, and by 0.64 days in the RCP85 run, compared to the PD run.

The TC motion speeds simulated in the PD run over the SP are generally slower than those observed south of 15°S (Figs. 6e,f). The mean TC motion speed in observations is $5.6\,\mathrm{m\,s^{-1}}$, but only $4.2\,\mathrm{m\,s^{-1}}$ in the PD run, and TCs tend to move southward. The area-averaged future change in translational speed in the RCP45 run is very small mostly due to the unevenly distributed change (Fig. 6g). In contrast, the area-averaged future change in translational speed in the RCP85 run is $0.52\,\mathrm{m\,s^{-1}}$ (Fig. 6h). Despite the overall acceleration of TCs in the RCP85 run (Fig. 6h), TCs show a general deceleration west of 165°E, while in most areas east of 165°E TCs show faster motion under the RCP85 scenario. Interestingly, the mean TC lifetime slightly increases in the warming runs, approximately by 0.2 days in the RCP45 run and 0.31 days in the RCP85 run. Combined with the averaged mean TC motion speed, we can speculate that TCs would travel a longer distance on average in the warmer world over the SP.

The vectors in Fig. 7 show future changes in the simulated mass-weighted, large-scale steering flows between the 850 and 300 hPa for JASO over the WP and JFMA over the SP. The hatched areas in Figs. 7a and 7b indicate the future changes that are not statistically significant at the 90% confidence level. The simulated future steering flow changes are remarkably different

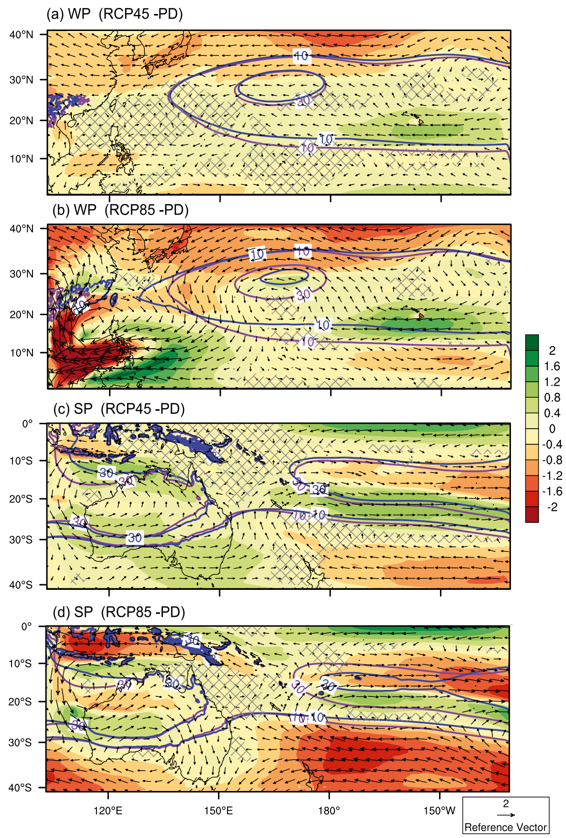

FIG. 7. The simulated future changes in the mass-weighted flows (vectors; m s^{-1}) and the departures of mean geopotential height at 500 hPa [colored contours; units: m; purple (blue) is for PD (RCP45 or RCP85)] during the peak season of (a),(b) JASO for the WP and (c),(d) JFMA for the SP. The shading indicates the difference in magnitude of the vectors (m s^{-1}) between the future (RCP45 and RCP85) and PD runs. The departure of mean geopotential height is calculated as the difference from the regional mean for the PD (purple) and future (blue) runs. The hatched areas indicate the vector differences of both the zonal and meridional components not statistically significant at the 90% confidence level.

from those shown in Murakami et al. (2011). In their paper, the easterly flows south of 20°N and east of 130°E significantly weakened, resulting in a significant future "slow down" of the westward translational speed. However, the easterly steering flow between 10° and 25°N generally strengthens in our warming runs (Figs. 7a,b). Note that Murakami et al. (2011) used IPCC Special Report on Emission Scenarios (SRES) A1B scenario in their study. The patterns of the future steering flow changes in the RCP45 and RCP85 runs are very similar (e.g., acceleration over the tropical regions and deceleration over the midlatitudes), but the changes in the RCP85 run are larger than those in the RCP45 run. The purple (blue) lines in Fig. 7 show the departures of the seasonal mean geopotential height at 500 hPa for the PD (future warming) runs. The western North Pacific subtropical high shrinks at its southern boundary in the warming runs, which causes the easterly winds shift northward. The westward extension of the subtropical high in the RCP85 run causes the westward retreat of the western Pacific monsoon trough. The steering flow changes are generally consistent with changes in TC translation. The SP subtropical high retreats and shrinks, leading to the increase in the westerly steering flow near 20°S (Figs. 7c,d) and resulting in the "speeding up" of TCs east of 165°E (Figs. 6g,h).

b. *The future changes in TC genesis*

Although GPI and its change do not perfectly agree with the TC genesis frequency and its change, GPI can still be used to identify the possible mechanisms that contribute to the future changes in TC genesis (Murakami et al. 2011). The white contour in Fig. 8a is the simulated GPI in the PD run (starts from 1 with interval of 2). Compared to the TC genesis map in Fig. 5a, the GPI is obviously too high over the South China Sea and in the ITCZ east of 170°W. Figure 8 shows the total future GPI changes during JASO over the WP (Figs. 8a,g), as well as the GPI changes induced by individual GPI factors (Figs. 8b–f,h–l). The sum of all individual GPI changes is approximately equivalent to the total GPI change. The hatched areas in Fig. 8 indicate the future changes that are not statistically significant at the 90% confidence level. Overall, the pattern for the future change in GPI is more similar to the future change in TC genesis frequency in the RCP85 run than that in the RCP45 run.

In the RCP45 run, relative humidity (Fig. 8c) and MPI (Fig. 8d) are two major factors that contribute positively to the increase in GPI in most of the WP region, and vertical wind shear has a positive contribution locally (Fig. 8e), while both relative vorticity (Fig. 8b) and vertical motion (Fig. 8f) reduce the GPI locally. The contribution by relative humidity in this study is very different from the results of Murakami et al. (2011), who reported that relative humidity had a very large negative contribution to the GPI change and tended to cancel the positive contribution by MPI. By contrast, Wu et al. (2014) reported that relative humidity had a small positive contribution to the GPI change in the warmer climate. Note that both Murakami et al. (2011) and Wu et al. (2014) used SRES A1B scenarios. The basic pattern in GPI changes for RCP85 (Figs. 8g–l) is similar to that for RCP45 (Figs. 8a–f) except that the region with GPI reduction in the western part of the WP is larger and more significant for the former than for the

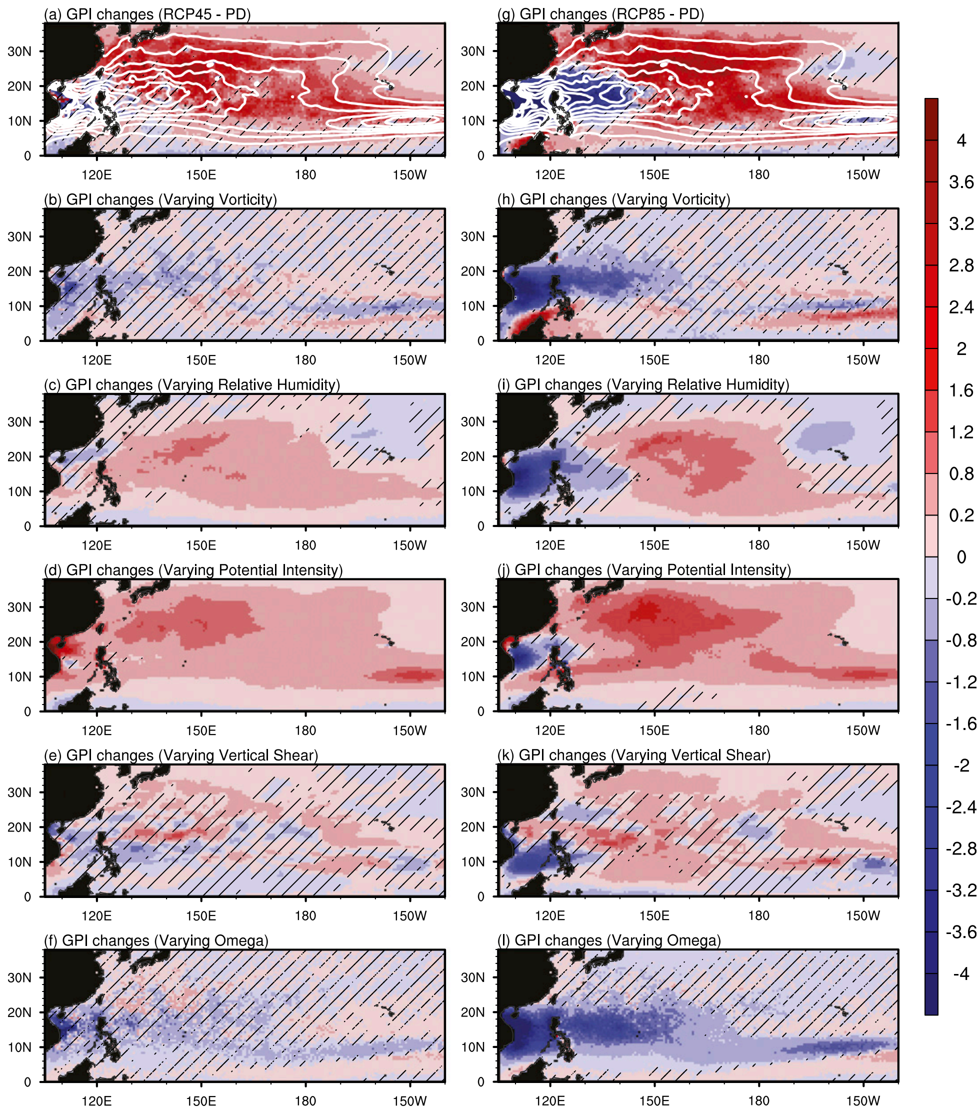

FIG. 8. (a),(g) Future change in GPI during JASO over the WP relative to the PD run, and GPI changes induced by each individual factor: (b),(h) vorticity, (c),(i) relative humidity, (d),(j) potential intensity, (e),(k) vertical wind shear, and (f),(l) vertical motion, for the (left) RCP45 and (right) RCP85 runs. The white contours in (a) are the simulated GPI in the PD run. The contour starts at 1 and ends at 21 with an interval of 2. The hatched areas indicate where future change is not significant at the 90% confidence level.

latter. Relative vorticity (Fig. 8h) and vertical motion (Fig. 8l) mainly have large negative contributions to the GPI change.

The maximum GPI in the PD run is located between 10° and 20°S over the SP (Fig. 9a, white contour), consistent with the TC genesis locations (Figs. 2b and 5a). The region with a statistically significant increase in GPI in the RCP45 run is mainly located north of 10°S, which is not the major TC genesis region, while the region with the statistically significant decrease in GPI is located east of 160°W. The region with the statistically significant decrease of TC genesis in the RCP45 has statistically insignificant changes in GPI (Figs. 9a and 5b). Both relative humidity and MPI changes contribute to the increase in GPI except for the area east of 160°W where the contribution by relative humidity is negative (Figs. 9c,d). The vertical wind shear is the major factor that reduces GPI south of 15°S (Fig. 9e). The change in

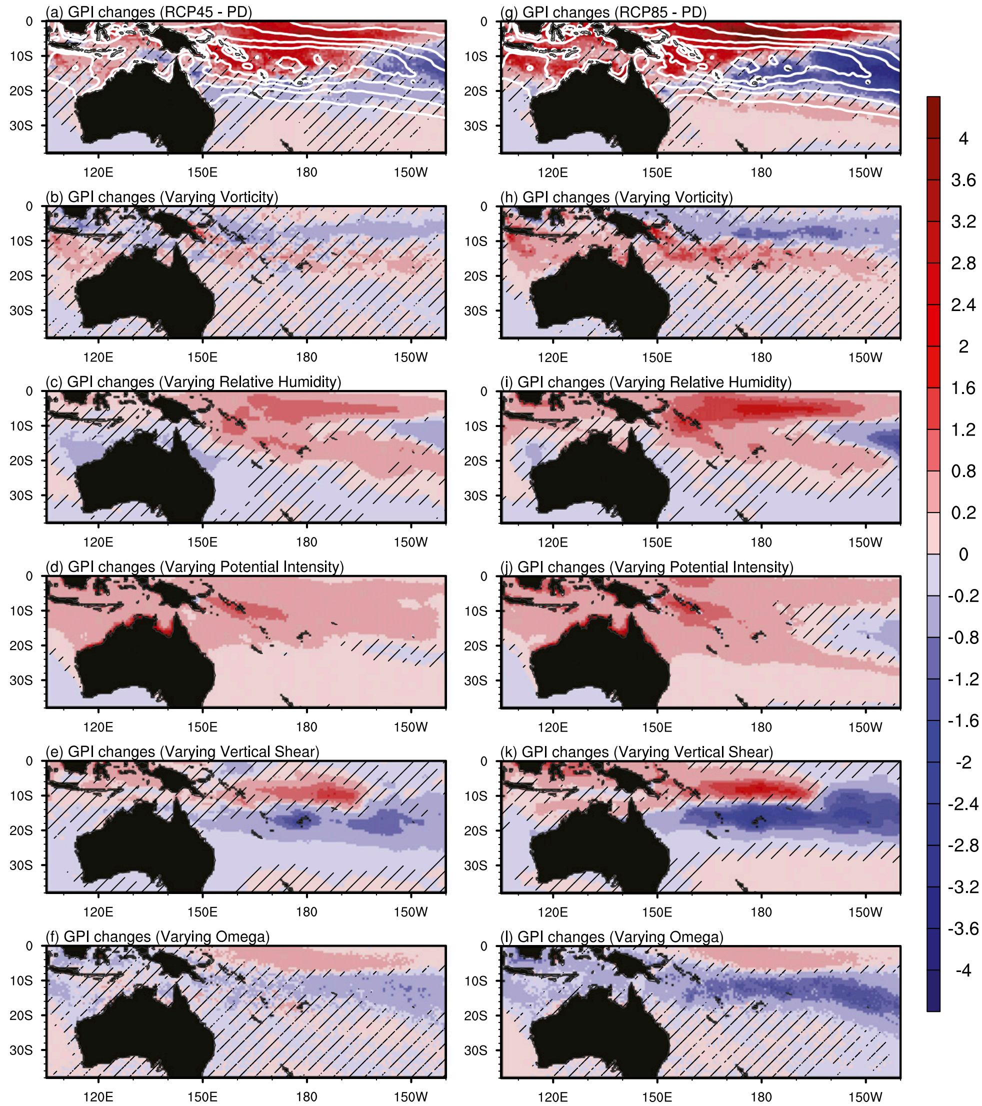

FIG. 9. As in Fig. 8, but for the SP.

vertical motion also reduces GPI between 10° and 15°S in the RCP45 run. The GPI change in the RCP85 run is much larger and more significant than that in the RCP45 run despite the similar spatial patterns for the two scenarios (Fig. 9g). The area with statistically significant reduction of GPI extends westward to 170°E (Fig. 9g). Similar to that in the RCP45 run, the vertical wind shear is the major contributor to the reduction in GPI south of 15°S and west of 160°W. For the GPI east of 160°W (Figs. 2 and 9g), relative humidity, MPI, vertical wind shear, and vertical motion are all unfavorable for GPI (Figs. 9h–l), leading to a significant decrease in TC genesis frequency over the SP as shown in Fig. 5c.

c. The simulated PD and future changes of large-scale circulations in JASO

Previous studies (e.g., Yokoi and Takayabu 2009; Murakami et al. 2011; Yokoi et al. 2012; Wu et al. 2014) have shown that the eastward shift of the WP monsoon trough was a possible cause of the increase in TC genesis in the eastern part of the WP. Instead of shifting eastward, here we show that the WP monsoon trough shifted westward in the strong greenhouse gases forcing in the RCP85 run. Figure 10 shows the 20-yr mean streamlines at 850 hPa in JASO. The model simulated WP monsoon trough in the PD run (Fig. 10b) is obviously too strong

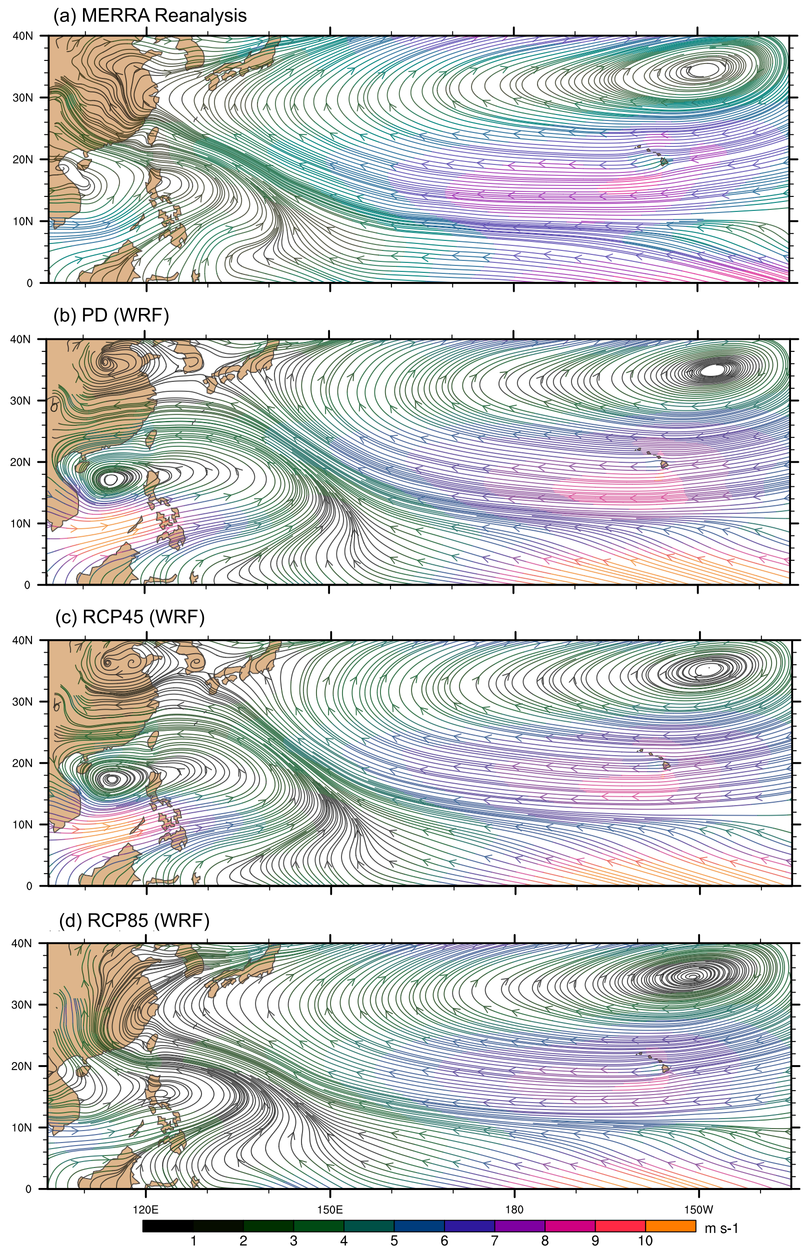

FIG. 10. The 850-hPa streamlines in JASO (a) from the MERRA reanalysis data, and from the model simulations in the (b) PD, (c) RCP45, and (d) RCP85 runs.

compared to that in the driving fields (Fig. 10a) and is about 10 degrees to the east and reaches 150°E. The "too strong" monsoon trough is also reported by Stowasser et al. (2007) in their simulations by using a high-resolution regional climate model (see their Fig. 2). In their future 6-times carbon dioxide simulation the monsoon trough is similar to that in PD simulation. In contrast, the monsoon trough is weaker in the simulations than observations by Wu et al. (2014, see their Fig. 9) with the Geophysical Fluid Dynamics Laboratory (GFDL) Regional Atmospheric Model (ZETAC). There is no large change in our RCP45 run (Fig. 10c). Nevertheless, the WP monsoon trough in the RCP85 run (Fig. 10d) retreats westward to near 140°E and the

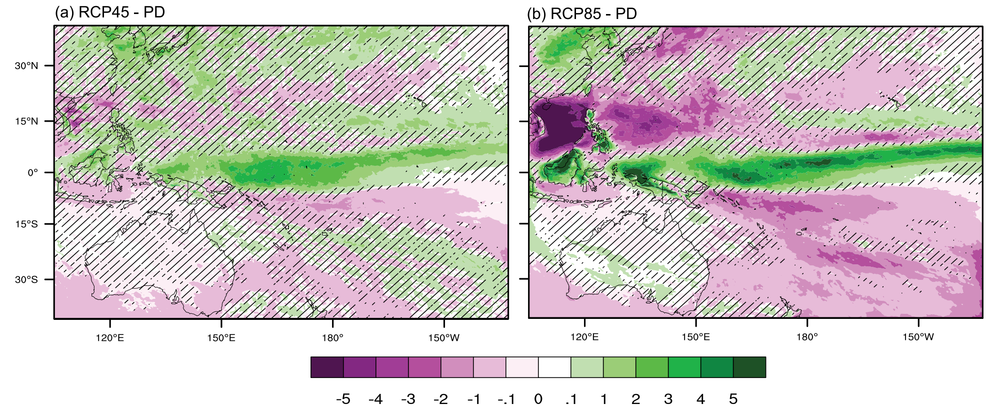

FIG. 11. The simulated future changes of precipitation in JASO for the (a) RCP45 and (b) RCP85 runs. The hatched areas indicate where the future change is not significant at the 90% confidence level.

subtropical high extends westward and occupies the northern part of the South China Sea. This indicates that the location of the WP monsoon trough might have a nonlinear response to the strength of the global warming forcing. The "moderate" forcing (e.g., RCP45) is not strong enough to significantly influence the WP monsoon trough or even shifts the monsoon trough slightly eastward (e.g., A1B; Murakami et al. 2011; Wu et al. 2014) or southeastward (e.g., A1B; Manganello et al. 2014), while the "strong" forcing shows a notable suppression of the WP monsoon trough and shifts it westward. However, the WP monsoon trough did not show any significant change in the ensemble mean of the CMIP5 12 model simulations for both RCP45 and RCP85 (figures not shown). Therefore, it remains an open question how the WP monsoon trough will change in the strong warming climate forcings. The recent study by Zong and Wu (2015) showed that TC formation events within the monsoon trough account for 43.1% of the total TC formation events in the WNP. The future change of TCs can be partially explained by the change of the western Pacific monsoon trough. The bias of the monsoon trough in the simulations might cause some uncertainties of the projected TC activities.

The future changes of precipitation by RCP45 and RCP85 are shown in Fig. 11. Both RCP45 and RCP85 result in a significant increase of precipitation in the central equatorial Pacific and the central Pacific around 15°N. The reduction of precipitation in RCP85 is associated with the retreat of the monsoon trough in RCP85. Another distinct feature of the precipitation change in RCP85 is that there is a significant increase of precipitation over the Maritime Continent, which may further cause the reduction of precipitation over South China Sea and Philippine Seas.

One possible explanation of the westward retreat of the WP monsoon trough in the RCP85 run is the change of zonal atmospheric circulation (namely, the weakening of the Walker Circulation). Figures 12a–c show the vectors of zonal wind and vertical velocity for the PD run and the

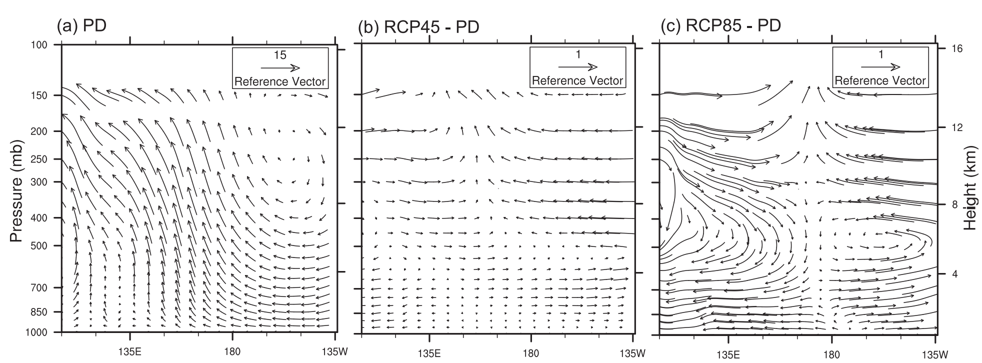

FIG. 12. (a) The vectors of zonal wind and vertical velocity for the PD run, and changes for the (b) RCP45 and (c) RCP85 runs, respectively. The winds are meridionally averaged between 10°S and 10°N. The Maritime Continent is excluded in the calculation.

changes in the RCP45 and RCP85 runs, respectively. The upward motion west of the date line and the downward motion east of 150°W are clearly presented in Fig. 12a. The change of the circulation is quite small in the RCP45 run (Fig. 12b). However, the change is much more significant in the RCP85 run (Fig. 12c). The intensified equatorial precipitation (Fig. 11b) over the central-eastern Pacific is associated with the reduced overall subsidence. As a result, the Walker circulation weakens and convection can be suppressed over the western part of the WP, which would lead to the weakening and the westward retreat of the WP summer monsoon trough. More warming in the central-eastern equatorial Pacific than in the western Pacific in response to global warming could favor stronger convection in the central-eastern Pacific and suppressed convection in the western part of the WP, leading to the weakening of both the Walker circulation and the WP summer monsoon trough and the reduction of TC genesis over the WP, in particular in the western part of the WP.

5. Summary

We used a 20-km mesh resolution regional climate model [the Advanced Research WRF (WRF-ARW) Model] with a newly improved Tiedtke cumulus parameterization scheme to conduct a pair of 20-yr simulations for the present day (PD; 1990–2009) and for the late twenty-first century (2080–99) under global warming conditions with two scenarios (RCP45 and RCP85) and studied the possible future changes of TC activities over both the WP and the SP.

The evaluation of the PD simulation demonstrates that the WRF Model performed reasonably well in reproducing the climatological mean, seasonal cycle, and interannual variations of TC activity over both the WP and the SP. The major biases include the slight shift of the peak month from August to September, the missing of very strong TCs ($>52\,\mathrm{m\,s^{-1}}$), and the overestimated TC frequency over the SP.

Results show that there is little change of TC genesis frequency over the whole WP defined in this study in the RCP45 run, but some regional changes are unevenly distributed. This is because the overall reduction of TC genesis frequency over the western part of the WP is compensated by the overall increase of TC genesis frequency over the eastern part. Similar changes are found for the frequency of TC occurrence and the ACE. The extent of the decrease in TC genesis frequency over the western part of the WP is much larger than that of the increase over the eastern part in the RCP85 run. As a result, the annual mean TC genesis frequency decreased from 25.90 in the PD and RCP45 runs to 21.65 in the RCP85 run over the whole WP. The eastward shift in TC genesis frequency and TC occurrence frequency is consistent with findings in other studies (e.g., Yokoi and Takayabu 2009; Murakami et al. 2011; Yokoi et al. 2012). The 20-yr mean TC genesis frequency over the SP consistently decreased from the RCP45 run to the RCP85 run. The future change in TC genesis frequency in the peak season is not significant in the WP for both RCP45 and RCP85 runs, but it decreased significantly in the peak season in the SP.

The occurrence frequency of weak TCs significantly decreased in the future warming runs over the WP, especially in the RCP85 run. Because of the limit of the model horizontal resolution, and possibly the dynamical core and physics parameterization schemes that we used, the maximum surface wind speed is not higher than $52\,\mathrm{m\,s^{-1}}$ in our simulations. Nevertheless, the TC frequency with wind speeds higher than $42.5\,\mathrm{m\,s^{-1}}$ is higher in the future runs over the WP. The frequency of TC occurrence over the SP decreases at all intensities in the future runs mostly due to the large reduction of TC genesis frequency under warmer climate conditions. There will be more strong TCs among the total TCs over both the WP and the SP in terms of the lifetime maximum near-surface wind speed.

We show that the projected changes in TC occurrence frequency can be explained by changes in steering flow and genesis location. A comparison of the steering flow in the PD run and the warming runs revealed that there are generally easterly anomalies between 10° and 25°N over the WP, resulting in acceleration of the westward moving TCs. The TCs formed in the southeast quadrant of the WP have a higher chance of recurving and moving northward with relatively higher translational speeds. As a result, the lifetime decreases more than half days in the RCP85 run over the WP. The increase in the westerly steering flow near 20°S is primarily due to the retreat and shrinking of the subtropical high over the SP, leading to the ''speeding up'' of TCs east of 165°E. In spite of the mean faster motion over the SP, the mean TC lifetime is slightly longer in the warming runs, indicating the averaged longer travel distance under the warmer conditions.

The projected changes in TC genesis frequency and location were analyzed in terms of GPI. The future changes in low-level relative vorticity, relative humidity, and vertical motion contributed to the reduction of GPI over the western part of the main TC genesis region over the WP, while relative humidity and MPI contributed to the increase in GPI over the eastern part of the main TC genesis region. Different from the WP, vertical wind shear and vertical motion contributed significantly to the decrease in GPI over the SP. Overall, the projected changes of TC activity under the RCP45 scenario are not as significant as those under the RCP85 scenario, as seen from the significance tests.

The reduction of GPI over the western part of the WP was found to be associated with the westward retreat and weakening of the WP monsoon trough in the RCP85 run. This is mainly due to the intensified equatorial convection associated with the larger warming over the central-eastern Pacific, which suppresses the overall upward motion and convection in the western part of the WP, leading to the weakening of the Walker circulation and weakening the WP monsoon trough, thus suppressing TC genesis in strong future warming forcing.

Finally we would point out that our projections are incomplete mainly due to the underestimated very strong TCs. Nevertheless, this study is among the first to provide projected changes in TC activity over the WP and the SP under two scenarios and the results demonstrate that in addition to the basin-scale future changes, regional changes are also important in response to possible anthropogenic forcing. Some of our results need to be further confirmed with higher-resolution model simulations in future studies.

Acknowledgments. The authors thank the two anonymous reviewers for their constructive review comments. This study was financially supported by the Department of Interior Pacific Islands Climate Science Center Agreements G12AC20501 and G13AC00363 awarded through the U.S. Geological Survey. We would like to acknowledge the Information Technology Services at University of Hawaii for providing access to their high performance computing facilities. We acknowledge the World Climate Research Programme's Working Group on Coupled Modelling, which is responsible for CMIP, and we thank the climate modeling groups (listed in Table 1 of this paper) for producing and making available their model outputs. For CMIP the U.S. Department of Energy's Program for Climate Model Diagnosis and Intercomparison provides coordinating support and leads development of software infrastructure in partnership with the Global Organization for Earth System Science Portals.

APPENDIX

A Brief Introduction to the New Modified Tiedtke Scheme

The new modified Tiedtke scheme has many improvements to the previous version of the modified Tiedtke scheme implemented into the WRF-ARW Model since version 3.3 (Zhang et al. 2011). The new modified Tiedtke scheme is improved mainly based on the ECMWF Integrated Forecasting System (IFS) documentation Cy40r1 (http://www.ecmwf.int/en/forecasts/documentation-and-support/changes-ecmwf-model/cycle-40r1/cycle-40r1). The new modified Tiedtke scheme can largely improve the simulations on tropical variations as well as the diurnal cycle of precipitation. Major improvements or the differences from those documented in the ECMWF IFS documentation include the following:

1) New trigger functions for deep and shallow convection initiations (Bechtold et al. 2004, 2008, 2014). In the WRF-ARW Model, the entrainment rate $\varepsilon_{\mathrm{up}}^{\mathrm{ini}}$ for testing parcel for shallow convection is $\varepsilon_{\mathrm{up}}^{\mathrm{ini}} = [(0.8/z) + 2\times10^{-4}]$, where z is the height, and for deep convection is $\varepsilon_{\mathrm{up}}^{\mathrm{ini}} = \varepsilon_{\mathrm{up}}^{(1)}[q_{\mathrm{sat}}(\overline{T})/q_{\mathrm{sat}}(\overline{T}_{\mathrm{depart}})]^3$, where $\varepsilon_{\mathrm{up}}^{(1)}$ is the entrainment rate in the updraft plume and $q_{\mathrm{sat}}(\overline{T})$ is the saturated water vapor at environment temperature T, and $q_{\mathrm{sat}}(\overline{T}_{\mathrm{depart}})$ is the saturated water vapor at departure level.
2) New convection closures for shallow and deep convection as introduced in Bechtold et al. (2014).
3) New convection time scale τ for deep convection (Bechtold et al. 2008). In the WRF-ARW Model, $\tau = (1 + 1.33\times10^{-5}\,dx)(H/\overline{w}_{\mathrm{up}})$, $720\,\mathrm{s} \le \tau \le 10800\,\mathrm{s}$, H is the cloud thickness, $\overline{w}_{\mathrm{up}}$ is the averaged updraft velocity in the cloud, and dx is the model horizontal resolutions in meters.
4) New entrainment and detrainment rates for all types of convection including shallow, deep, and midlevel convections (Bechtold et al. 2008).
5) New formula for the conversion from cloud water/ice to rain/snow (Sundqvist 1978).
6) New method to include the convection-induced pressure gradients associated with the convective momentum transport. The pressure gradients are mimicked by doubling the detrainment rate in ECMWF IFS. We applied the method from Wu and Yanai (1994) and Gregory et al. (1997). The convection-induced pressure gradient force (PGF) is parameterized as $\mathrm{PGF} = -cM_u[(1/\overline{\rho})(\partial\overline{V}/\partial z)]$, where M_u is updraft mass flux, $\overline{\rho}$ is air density, $\overline{V}$ is environmental wind speed, z is height, and c is the tunable coefficient; 0.7 is an optimal value currently used in the WRF-ARW Model.

REFERENCES

Bechtold, P., J. P. Chaboureau, A. C. M. Beljaars, A. K. Betts, M. Kohler, M. Miller, and J. L. Redelsperger, 2004: The simulation of the diurnal cycle of convective precipitation over land in global models. *Quart. J. Roy. Meteor. Soc.*, **130**, 3119–3137, doi:10.1256/qj.03.103.

——, M. Köhler, T. Jung, F. Doblas-Reyes, M. Leutbecher, M. Rodwell, F. Vitart, and G. Balsamo, 2008: Advances in predicting atmospheric variability with the ECMWF model: From synoptic to decadal time-scales. *Quart. J. Roy. Meteor. Soc.*, **134**, 1337–1351, doi:10.1002/qj.289.

——, N. Semane, P. Lopez, J.-P. Chaboureau, A. Beljaars, and N. Bormann, 2014: Representing equilibrium and nonequilibrium convection in large-scale models. *J. Atmos. Sci.*, **71**, 734–753, doi:10.1175/JAS-D-13-0163.1.

Bengtsson, L., K. I. Hodges, and M. Esch, 2007a: Tropical cyclone in a T159 resolution global model: Comparison with observations and re-analyses. *Tellus*, **59A**, 396–416, doi:10.1111/j.1600-0870.2007.00236.x.

——, ——, ——, N. Keenlyside, L. Kornblueh, J.-J. Luo, and T. Yamagata, 2007b: How may tropical cyclones change in a warmer climate? *Tellus*, **59A**, 539–561, doi:10.1111/j.1600-0870.2007.00251.x.

Camargo, S. J., 2013: Global and regional aspects of tropical cyclone activity in the CMIP5 models. *J. Climate*, **26**, 9880–9902, doi:10.1175/JCLI-D-12-00549.1.

Chen, F., and J. Dudhia, 2001: Coupling an advanced land surface–hydrology model with the Penn State–NCAR MM5 modeling system. Part I: Model implementation and sensitivity. *Mon. Wea. Rev.*, **129**, 569–585, doi:10.1175/1520-0493(2001)129<0569:CAALSH>2.0.CO;2.

Colbert, A. J., B. J. Soden, and B. P. Kirtman, 2015: The impact of natural and anthropogenic climate change on western North Pacific tropical cyclone tracks. *J. Climate*, **28**, 1806–1823, doi:10.1175/JCLI-D-14-00100.1.

Dee, D. P., and Coauthors, 2011: The ERA-Interim reanalysis: Configuration and performance of the data assimilation system. *Quart. J. Roy. Meteor. Soc.*, **137**, 553–597, doi:10.1002/qj.828.

Done, J., G. Holland, C. Bruyère, L. Leung, and A. Suzuki-Parker, 2015: Modeling high-impact weather and climate: Lessons from a tropical cyclone perspective. *Climatic Change*, **129**, 381–395, doi:10.1007/s10584-013-0954-6.

Emanuel, K. A., 1995: Sensitivity of tropical cyclones to surface exchange coefficients and a revised steady-state model incorporating eye dynamics. *J. Atmos. Sci.*, **52**, 3969–3976, doi:10.1175/1520-0469(1995)052<3969:SOTCTS>2.0.CO;2.

——, 2013: Downscaling CMIP5 climate models shows increased tropical cyclone activity over the 21st century. *Proc. Natl. Acad. Sci. USA*, **110**, 12 219–12 224, doi:10.1073/pnas.1301293110.

——, and D. S. Nolan, 2004: Tropical cyclone activity and global climate. Preprints, *26th Conf. on Hurricanes and Tropical Meteorology*, Miami, FL, Amer. Meteor. Soc., 240–241.

Gregory, D., R. Kershaw, and P. M. Inness, 1997: Parameterization of momentum transport by convection. II: Tests in single-column and general circulation models. *Quart. J. Roy. Meteor. Soc.*, **123**, 1153–1183, doi:10.1002/qj.49712354103.

Hashimoto, A., J. M. Done, L. D. Fowler, and C. L. Bruyère, 2016: Tropical cyclone activity in nested regional and global grid-refined simulations. *Climate Dyn.*, **47**, 497–508, doi:10.1007/s00382-015-2852-2.

Held, I. M., and M. Zhao, 2011: The response of tropical cyclone statistics to an increase in CO_2 with fixed sea surface temperatures. *J. Climate*, **24**, 5353–5364, doi:10.1175/JCLI-D-11-00050.1.

Hong, S.-Y., and J.-O. J. Lim, 2006: The WRF single-moment microphysics scheme (WSM6). *J. Korean Meteor. Soc.*, **42**, 129–151.

——, Y. Noh, and J. Dudhia, 2006: A new vertical diffusion package with an explicit treatment of entrainment processes. *Mon. Wea. Rev.*, **134**, 2318–2341, doi:10.1175/MWR3199.1.

Iacono, M. J., J. S. Delamere, E. J. Mlawer, M. W. Shephard, S. A. Clough, and W. D. Collins, 2008: Radiative forcing by long-lived greenhouse gases: Calculations with the AER radiative transfer models. *J. Geophys. Res.*, **113**, D13103, doi:10.1029/2008JD009944.

Jin, C.-S., D.-H. Cha, D.-K. Lee, M.-S. Suh, S.-Y. Hong, H.-S. Kang, and C.-H. Ho, 2016: Evaluation of climatological tropical cyclone activity over the western North Pacific in the CORDEX-East Asia multi-RCM simulations. *Climate Dyn.*, **47**, 765–778, doi:10.1007/s00382-015-2869-6.

Jourdain, N. C., P. Marchesiello, C. E. Menkes, J. Lefèvre, E. M. Vincent, M. Lengaigne, and F. Chauvin, 2011: Mesoscale simulation of tropical cyclones in the South Pacific: Climatology and interannual variability. *J. Climate*, **24**, 3–25, doi:10.1175/2010JCLI3559.1.

Jullien, S., P. Marchesiello, C. E. Menkes, J. Lefèvre, N. C. Jourdain, G. Samson, and M. Lengaigne, 2014: Ocean feedback to tropical cyclones: Climatology and processes. *Climate Dyn.*, **43**, 2831–2854, doi:10.1007/s00382-014-2096-6.

Kain, J., 2004: The Kain–Fritsch convective parameterization: An update. *J. Appl. Meteor.*, **43**, 170–181, doi:10.1175/1520-0450(2004)043<0170:TKCPAU>2.0.CO;2.

Kawase, H., T. Yoshikane, M. Hara, F. Kimura, T. Yasunari, B. Ailikun, H. Ueda, and T. Inoue, 2009: Intermodel variability of future changes in the Baiu rainband estimated by the pseudo global warming downscaling method. *J. Geophys. Res.*, **114**, D21110, doi:10.1029/2009JD011803.

Kim, D., C.-S. Jin, C.-H. Ho, J. Kim, and J.-H. Kim, 2015: Climatological features of WRF-simulated tropical cyclones over the western North Pacific. *Climate Dyn.*, **44**, 3223–3235, doi:10.1007/s00382-014-2410-3.

Kimura, F., and A. Kitoh, 2007: Downscaling by pseudo-global warming method. Final REPORT of the ICCAP, RIHN Project 1-1, 43–46. [Available online at www.chikyu.ac.jp/P-C09/ICCAP/ICCAP_Final_Report/2/4-climate_kimura.pdf.]

Kinter, J. L., III, and Coauthors, 2013: Revolutionizing climate modeling with project Athena: A multi-institutional, international collaboration. *Bull. Amer. Meteor. Soc.*, **94**, 231–245, doi:10.1175/BAMS-D-11-00043.1.

Knapp, K. R., M. C. Kruk, D. H. Levinson, H. J. Diamond, and C. J. Neumann, 2010: The International Best Track Archive for Climate Stewardship (IBTrACS): Unifying tropical cyclone data. *Bull. Amer. Meteor. Soc.*, **91**, 363–376, doi:10.1175/2009BAMS2755.1.

Knutson, T. R., and R. E. Tuleya, 2004: Impact of CO_2-induced warming on simulated hurricane intensity and precipitation: Sensitivity to the choice of climate model and convective parameterization. *J. Climate*, **17**, 3477–3495, doi:10.1175/1520-0442(2004)017<3477:IOCWOS>2.0.CO;2.

——, ——, and Y. Kurihara, 1998: Simulated increase of hurricane intensities in a CO_2-warmed climate. *Science*, **279**, 1018–1021, doi:10.1126/science.279.5353.1018.

——, J. J. Sirutis, S. T. Garner, I. M. Held, and R. E. Tuleya, 2007: Simulation of the recent multidecadal increase of Atlantic hurricane activity using an 18-km-grid regional model. *Bull. Amer. Meteor. Soc.*, **88**, 1549–1565, doi:10.1175/BAMS-88-10-1549.

——, ——, ——, G. A. Vecchi, and I. M. Held, 2008: Simulated reduction in Atlantic hurricane frequency under twenty-first-century warming conditions. *Nat. Geosci.*, **1**, 359–364, doi:10.1038/ngeo202.

——, and Coauthors, 2010: Tropical cyclones and climate change. *Nat. Geosci.*, **3**, 157–163, doi:10.1038/ngeo779.

——, J. J. Sirutis, M. Zhao, R. E. Tuleya, M. Bender, G. A. Vecchi, G. Villarini, and D. Chavas, 2015: Global projections of intense tropical cyclone activity for the late twenty-first century from dynamical downscaling of CMIP5/RCP4.5 scenarios. *J. Climate*, **28**, 7203–7224, doi:10.1175/JCLI-D-15-0129.1.

Lauer, A., C. Zhang, O. Elison-Timm, Y. Wang, and K. Hamilton, 2013: Downscaling of climate change in the Hawaii region using CMIP5 results: On the choice of the forcing fields. *J. Climate*, **26**, 10 006–10 030, doi:10.1175/JCLI-D-13-00126.1.

Lavender, S. L., and K. J. E. Walsh, 2011: Dynamically downscaled simulations of Australian region tropical cyclones in current and future climates. *Geophys. Res. Lett.*, **38**, L10705, doi:10.1029/2011GL047499.

Li, T., M. Kwon, M. Zhao, J.-S. Kug, J.-J. Luo, and W. Yu, 2010: Global warming shifts Pacific tropical cyclone location. *Geophys. Res. Lett.*, **37**, L21804, doi:10.1029/2010GL045124.

Manganello, J. V., and Coauthors, 2012: Tropical cyclone climatology in a 10-km global atmospheric GCM: Toward weather-resolving climate modeling. *J. Climate*, **25**, 3867–3893, doi:10.1175/JCLI-D-11-00346.1.

——, and Coauthors, 2014: Future changes in the western North Pacific tropical cyclone activity projected by a multidecadal simulation with a 16-km global atmospheric GCM. *J. Climate*, **27**, 7622–7646, doi:10.1175/JCLI-D-13-00678.1.

McDonald, J. H., 2014: *Handbook of Biological Statistics*. 3rd ed. Sparky House Publishing, 299 pp.

Murakami, H., and B. Wang, 2010: Future change of North Atlantic tropical cyclone tracks: Projection by a 20-km-mesh global atmospheric model. *J. Climate*, **23**, 2699–2721, doi:10.1175/2010JCLI3338.1.

——, ——, and A. Kitoh, 2011: Future change of western North Pacific typhoons: Projections by a 20-km-mesh global atmospheric model. *J. Climate*, **24**, 1154–1169, doi:10.1175/2010JCLI3723.1.

——, and Coauthors, 2012: Future changes in tropical cyclone activity projected by the new high-resolution MRI-AGCM. *J. Climate*, **25**, 3237–3260, doi:10.1175/JCLI-D-11-00415.1.

——, B. Wang, T. Li, and A. Kitoh, 2013: Projected increase in tropical cyclones near Hawaii. *Nat. Climate Change*, **3**, 749–754, doi:10.1038/nclimate1890.

Nguyen, K. C., and K. J. E. Walsh, 2001: Interannual, decadal, and transient greenhouse simulation of tropical cyclone–like vortices in a regional climate model of the South Pacific. *J. Climate*, **14**, 3043–3054, doi:10.1175/1520-0442(2001)014<3043:IDATGS>2.0.CO;2.

Oouchi, K., J. Yoshimura, H. Yoshimura, R. Mizuta, S. Kusunoki, and A. Noda, 2006: Tropical cyclone climatology in a global-warming climate as simulated in a 20 km-mesh global atmospheric model: Frequency and wind intensity analysis. *J. Meteor. Soc. Japan*, **84**, 259–276, doi:10.2151/jmsj.84.259.

Reed, K. A., J. T. Bacmeister, M. F. Rosenbloom, N. A. Wehner, S. C. Bates, P. H. Lauritzen, J. T. Truesdale, and C. Hannay, 2015: Impact of the dynamical core on the direct simulation of tropical cyclones in a high-resolution global model. *Geophys. Res. Lett.*, **42**, 3603–3608, doi:10.1002/2015GL063974.

Reynolds, R. W., C. L. Gentemann, and G. K. Corlett, 2010: Evaluation of AATSR and TMI satellite SST data. *J. Climate*, **23**, 152–165, doi:10.1175/2009JCLI3252.1.

Rienecker, M. M., and Coauthors, 2011: MERRA: NASA's Modern-Era Retrospective Analysis for Research and Applications. *J. Climate*, **24**, 3624–3648, doi:10.1175/JCLI-D-11-00015.1.

Sato, T., F. Kimura, and A. Kitoh, 2007: Projection of global warming onto regional precipitation over Mongolia using a regional climate model. *J. Hydrol.*, **333**, 144–154, doi:10.1016/j.jhydrol.2006.07.023.

Skamarock, W. C., and Coauthors, 2008: A description of the Advanced Research WRF version 3. NCAR Tech. Note NCAR/TN-475+STR, 113 pp., doi:10.5065/D68S4MVH.

Stowasser, M., Y. Wang, and K. Hamilton, 2007: Tropical cyclone changes in the western North Pacific in a global warming scenario. *J. Climate*, **20**, 2378–2396, doi:10.1175/JCLI4126.1.

Sugi, M., H. Murakami, and J. Yoshimura, 2012: On the mechanism of tropical cyclone frequency changes due to global warming. *J. Meteor. Soc. Japan*, **90A**, 397–408, doi:10.2151/jmsj.2012-A24.

Sundqvist, H., 1978: A parameterization scheme for non-convective condensation including prediction of cloud water content. *Quart. J. Roy. Meteor. Soc.*, **104**, 677–690, doi:10.1002/qj.49710444110.

Villarini, G., and G. A. Vecchi, 2012: Twenty-first-century projections of North Atlantic tropical storms from CMIP5 models. *Nat. Climate Change*, **2**, 604–607, doi:10.1038/nclimate1530.

Walsh, K. J. E., 2015: Fine resolution simulations of the effect of climate change on tropical cyclones in the South Pacific. *Climate Dyn.*, **45**, 2619–2631, doi:10.1007/s00382-015-2497-1.

Wang, Y., O. L. Sen, and B. Wang, 2003: A highly resolved regional climate model (IPRC-RegCM) and its simulation of the 1998 severe precipitation events over China. Part I: Model description and verification of simulation. *J. Climate*, **16**, 1721–1738, doi:10.1175/1520-0442(2003)016<1721:AHRRCM>2.0.CO;2.

Wu, L., and Coauthors, 2014: Simulations of the present and late-twenty-first-century western North Pacific tropical cyclone activity using a regional model. *J. Climate*, **27**, 3405–3424, doi:10.1175/JCLI-D-12-00830.1.

Wu, X., and M. Yanai, 1994: Effects of vertical wind shear on the cumulus transport of momentum: Observations and parameterization. *J. Atmos. Sci.*, **51**, 1640–1660, doi:10.1175/1520-0469(1994)051<1640:EOVWSO>2.0.CO;2.

Yokoi, S., and Y. N. Takayabu, 2009: Multi-model projection of global warming impact on tropical cyclone genesis frequency over the western North Pacific. *J. Meteor. Soc. Japan*, **87**, 525–538, doi:10.2151/jmsj.87.525.

——, C. Takahashi, K. Yasunaga, and R. Shirooka, 2012: Multi-model projection of tropical cyclone genesis frequency over the western North Pacific: CMIP5 results. *SOLA*, **8**, 137–140, doi:10.2151/sola.2012-034.

Zhang, C., Y. Wang, and K. Hamilton, 2011: Improved representation of boundary layer clouds over the southeast Pacific in ARW-WRF using a modified Tiedtke cumulus parameterization scheme. *Mon. Wea. Rev.*, **139**, 3489–3513, doi:10.1175/MWR-D-10-05091.1.

——, ——, ——, and A. Lauer, 2016a: Dynamical downscaling of the climate for the Hawaiian Islands. Part I: Present day. *J. Climate*, **29**, 3017–3048, doi:10.1175/JCLI-D-15-0432.1.

——, ——, ——, and ——, 2016b: Dynamical downscaling of the climate for the Hawaiian Islands. Part II: Projection for the late twenty-first century. *J. Climate*, **29**, 8333–8354, doi:10.1175/JCLI-D-16-0038.1.

Zhao, M., I. M. Held, S.-J. Lin, and G. A. Vecchi, 2009: Simulations of global hurricane climatology, interannual variability, and response to global warming using a 50-km resolution GCM. *J. Climate*, **22**, 6653–6678, doi:10.1175/2009JCLI3049.1.

Zong, H., and L. Wu, 2015: Re-examination of tropical cyclone formation in monsoon troughs over the western North Pacific. *Adv. Atmos. Sci.*, **32**, 924–934, doi:10.1007/s00376-014-4115-2.